



# Temperature effect on irradiation damage in equiatomic multi-component alloys

Emil Levo<sup>a,\*</sup>, Fredric Granberg<sup>a,\*</sup>, Kai Nordlund<sup>a</sup>, Flyura Djurabekova<sup>a,b</sup>

<sup>a</sup> Department of Physics, P.O. Box 43, FIN-00014 University of Helsinki, Finland

<sup>b</sup> Helsinki Institute of Physics, P.O. Box 43, FIN-00014, University of Helsinki, Finland

## ARTICLE INFO

### Keywords:

High entropy alloy  
Temperature dependence  
Irradiation damage  
Molecular dynamics

## ABSTRACT

Multiphase designed concentrated solid solution alloys, such as high entropy alloys (HEA) and equiatomic multi-component alloys (EAMC-alloys) have shown much promise for use as structural components in future nuclear energy production concepts. The irradiation tolerance in these novel alloys has been shown to be superior to that in more conventional metals used in current nuclear reactors. However, studies involving irradiation of HEAs and EAMC-alloys have usually been performed at room temperature. Hence, in this study the irradiation damage is investigated computationally in two different Ni-based EAMC-alloys and pure Ni at four different temperatures, ranging from 138 K to 800 K. The irradiation damage was studied by analyzing point defects, defect cluster sizes and dislocation networks in the materials. Dislocation loop mobility calculations were performed to help understanding the formation of different dislocation networks in the irradiated materials. Utilizing the knowledge of the depth distribution of damage, and using simulations of Rutherford backscattering in channeling conditions (RBS/c), we can relate our results to experimental data. The main findings are that the alloys have superior irradiation tolerance at all temperatures as compared to pure Ni, and that the damage is reduced in all materials with an increase in temperature.

## 1. Introduction

New advancements in energy production, such as next generation nuclear reactors, have increased the need to develop novel materials able to withstand demanding operational environments in which high irradiation doses, high temperatures and corrosion risks are commonplace. High entropy alloys (HEA) are a relatively new group of materials, that have been extensively researched for their unique properties, with promising results regarding their possible utilization in nuclear reactors. There is no universally accepted definition of a HEA, but one of the most commonly used is that the alloy should be built of at least five different elements, where each element contributes with a roughly equal concentration (between 5–35 at.%) [1]. So called equiatomic multi-component alloys (EAMC-alloys) are a subgroup of HEA, where the number of elements is allowed to be less than five, but each element is present at equal concentrations. Even though EAMC-alloys can, for convenience, be called HEAs due to their maximized configurational entropy, we will distinguish EAMC-alloys and HEAs from one another in accordance with previous work [2–5].

The irradiation resistance in Ni-based HEAs and EAMC-alloys has

been studied both experimentally and computationally [6–8,2,3,9,4,10,5], with some of the results concluding that the alloys exhibit a heightened tolerance against irradiation when compared to pure Ni. Being subject to not only high irradiation doses but also high temperatures, the effect which different temperature has on the damage accumulation in HEAs should be investigated. The studies of the temperature dependence to date have been experimental [7,11–13]. These works have for instance shown that NiFe outperforms NiCoCr, in terms of irradiation tolerance, at temperatures above 300 K, while at temperatures below or equal to 300 K, the behaviour is opposite [11].

To understand the atom-level mechanisms underlying the temperature dependence, in this work we extend previous computational studies at room temperature [2,4] to a broader temperature range. We study the irradiation damage in Ni-based EAMC-alloys at four different temperatures: 138 K, 300 K, 500 K and 800 K. In addition to the defect number and cluster size evolution analyses, we also carry out simulations of Rutherford backscattering in channeling mode (RBS/c) on the samples, to be able to compare the results with experiments.

\* Corresponding authors.

E-mail addresses: [emil.levo@helsinki.fi](mailto:emil.levo@helsinki.fi) (E. Levo), [fredric.granberg@helsinki.fi](mailto:fredric.granberg@helsinki.fi) (F. Granberg).

<https://doi.org/10.1016/j.commsci.2021.110571>

Received 9 April 2021; Received in revised form 28 April 2021; Accepted 30 April 2021

Available online 26 May 2021

0927-0256/© 2021 The Authors. Published by Elsevier B.V. This is an open access article under the CC BY license (<http://creativecommons.org/licenses/by/4.0/>).

## 2. Methods

### 2.1. Irradiation simulation setup

The irradiation simulations have been conducted with the classical molecular dynamics code PARCAS [14,15]. Two different interatomic potentials were used to describe atomic interactions in the simulations. Both the Bonny et al. and Zhou et al. potentials [16,17] were used to describe separately Ni and NiFe, while NiCoCr was simulated by using a combination of the Zhou et al. potential for NiCo and the Lin et al. potential [18] for Cr, resulting in five different material samples. The use of the completely separately developed Bonny et al. and Zhou et al. potentials for Ni and NiFe allows to assess how sensitive the results are to the choice of interatomic potential. Electronic stopping power and the ZBL repulsive potential [19,20] were also used in combination with the potentials mentioned above, to accurately describe the high energy effects in the irradiation simulations.

The sample cells consisted of 256 000 atoms arranged in a face centered cubic (FCC) lattice, resulting in cell sizes of approximately  $14 \times 14 \times 14 \text{ nm}^3$ . Periodic boundary conditions were used in all dimensions. The atoms in the NiFe and NiCoCr samples were randomly ordered with equal concentrations of each element. Three sample cells were created for each material by re-ordering the atoms randomly (except for the pure Ni) so that three independent simulation series could be carried out. The sample cells were simulated at four different temperatures: 138 K, 300 K, 500 K and 800 K. This resulted in a total of 60 simulated systems (4 temperatures  $\times$  3 simulation series  $\times$  5 materials).

In each sample cell, an irradiation event was simulated by giving a central atom a recoil energy of 5 keV in a random direction, leading to a collision cascade in the system. During the first 20 ps after the initial recoil, the sample cells were cooled down in their border regions (slabs of  $4 \text{ \AA}$  on each side of the cell) with a Berendsen thermostat [21] to avoid overheating of the cells. Then, for an additional 10 ps, the whole cell was cooled with the Berendsen thermostat, and the pressure of the system was controlled with a Berendsen barostat [21]. 2000 such irradiation events were repeated in all cells, to achieve massively overlapping cascades. This adds up to a dose of roughly 0.3 dpa, with a threshold displacement energy of 40 eV, according to the NRT-dpa equation [22–24]. We use the original NRT-dpa without the arc-dpa correction [25,26] to enable comparison with experiments that also use the original NRT scaling. After each irradiation event, the cell was shifted randomly in all dimensions over the periodic boundaries [27], to achieve a homogeneous irradiation of the system.

Additionally, 100 single irradiation events were simulated for each material with each potential and temperature, with the same 5 keV recoil energy. This was done to investigate the early stages of the defect structure development.

### 2.2. Dislocation mobility simulations

The lower defect accumulation in HEAs and EAMC-alloys has been partly attributed to a lesser dislocation mobility in them [2–4]. Therefore, dislocation loop mobility simulations were conducted to complement the irradiation simulations. Two differently sized  $\langle 110 \rangle$  interstitial loops were created in FCC cells with an orientation of [110], [112] and [111] in the x-, y- and z-directions, respectively. The loops had radii of 5 Å and 10 Å. The loops were let to move freely in the cells for 5 ns at two different temperatures: 300 K and 600 K, i.e. the simulations test the random thermally activated mobility of dislocations. The materials were simulated utilizing the same potentials as in the irradiation simulations.

### 2.3. Analysis

The Wigner–Seitz cell method [14] was used to extract the number

and positions of point defects (interstitials and vacancies) in the samples after each subsequent irradiation event. This information was used with the help of OVITO:s cluster analysis modifier [28] to find out the defect cluster size distribution, number of defects in clusters and the segregation of different elements in interstitial type clusters (for the alloys). The cutoff used for the cluster analysis to consider atoms to belong to the same cluster was the distance from any atom belonging to the FCC lattice, to the midway point between its second and third nearest neighbour.

To analyze the stability of interstitial type defects, single  $\langle 100 \rangle$  dumbbell quenching calculations were performed. All permutations of the elements in the dumbbell were investigated in all alloys to obtain their formation energy. More details of the simulation can be found in the [Supplementary material online](#).

Dislocations in the irradiated samples and the dislocation mobility studies were analyzed with OVITO:s dislocation extraction algorithm modifier [29]. The position of the dislocation loops in the mobility studies were calculated by first calculating the average position of each dislocation segment based on their junction points. Then the average of these averages was calculated to get the final position of the loop.

### 2.4. Rutherford backscattering calculations

To be able to compare the simulated results directly with experiments, RBS/c calculations were carried out with the RBSADEC code [30]. We follow here the same approach that has previously been shown to result in good agreement with room temperature experiments [31]. To be able to perform the RBS/c calculations, the irradiated cells had to be merged together according to a nuclear energy deposition depth profile. The depth profile was calculated in Ni with the MDRANGE code [32] using  $\text{Ni}^+$  ions with a deposition energy of 1.5 MeV and a fluence of  $1.0 \times 10^{14} \text{ cm}^{-2}$ . The resulting profile can be seen in Fig. 1 with a peak damage dose of approximately 0.2 dpa at about 300 nm. This profile was used in the merging of the cells for all of the irradiated materials. The final merged cells consisted of 62 irradiated cells from the first 1000 cascades in each material, resulting in almost 900 nm long slabs.

In the calculations, 3.5 MeV  $\text{He}^+$  ions were used as the backscattering ions. The detector was set to a scattering angle of  $155^\circ$ , and the number of channels to 4096, with each channel corresponding to 1 keV. These parameters were chosen according to previous RBS/c experiments [33]. The temperature in the calculations was varied depending on whether the samples had been irradiated below or at room temperature ( $\leq 300 \text{ K}$ ), or above room temperature ( $> 300 \text{ K}$ ) according to previous experiment [11]. For the samples irradiated at room temperature or below it, the RBS/c calculations were ran at the irradiation temperatures. E.g. all materials irradiated at 138 K were also analysed at 138 K with

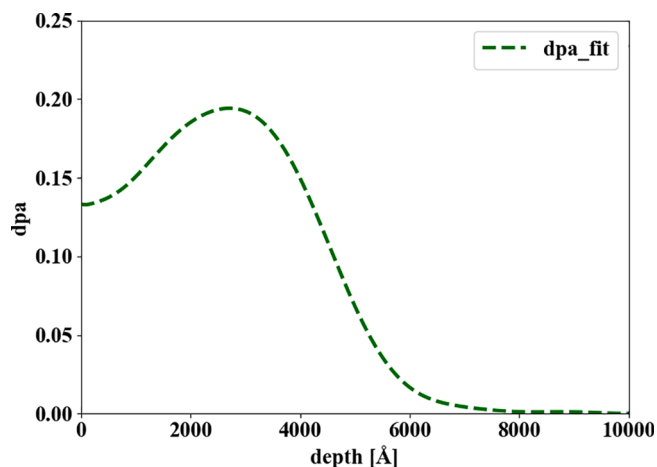


Fig. 1. Nuclear energy deposition profile in Ni.

RBSADEC. For the samples irradiated at above room temperature, the RBS/c calculations were ran at room temperature because this was also the case in the experiments. E.g. all materials irradiated at 800 K were analysed at 300 K. Each case of every material was analyzed to obtain three RBS/c spectra for each material. The mean damage profile for each material was obtained this way over the whole temperature range.

### 3. Results

#### 3.1. Point defect concentration

In Refs. 2 and 4 the point defect accumulation was compared at 300 K between different EAMC-alloys and pure Ni. It was seen that with an increased number of elements, a lesser defect accumulation occurred. In this paper, Figs. 2 and 3 show the temperature effect on the defect accumulation in each material, while Figs. 4 and 5 show conversely the material effect on the defect accumulation at each temperature.

The overall trend in all the subfigures of Figs. 2 and 3 is that with an increased temperature, the saturation level of accumulated point defects is lowered. From the figures we can see that pure Ni has about a factor two difference between the highest and lowest temperature saturation points, while the alloys have about a factor three difference. When comparing the two potentials with each other, the choice of potential seems to have little effect on the point defect accumulation for NiFe. For Ni, however, we can see that the defect concentration is much higher

with the Bonny et al. potential than with the Zhou et al. potential.

The comparison between materials (Figs. 4 and 5) show the same trend as seen before [2,4] at the lower temperatures (138 and 300 K), i.e. Ni has the worst irradiation tolerance, NiFe is better, and NiCoCr is the best. At the higher temperatures (500 and 800 K) where the alloys definitely perform better than pure Ni, it is unclear whether NiFe or NiCoCr performs best in terms of lower defect accumulation.

The point defect data for the single cascade simulations can be seen in Fig. 6. For the Zhou et al. potential, the plot shows the materials being ordered as NiFe, NiCoCr and Ni, going from most produced point defects to least at all temperatures. This confirms that the behaviour seen earlier at 300 K [4], holds up in the whole temperature range 138–800 K. For the Bonny et al. potential, Ni has more produced point defects than NiFe, at all temperatures. The amount of point defects decreases in all materials for both potentials, with the increase in temperature.

#### 3.2. Defect cluster size

The size evolution can be seen for interstitial type defect clusters in Fig. 7 and vacancy type defect clusters in Fig. 8 for the Zhou et al. NiCoCr at all investigated temperatures. The rest of the materials, including NiCoCr, at all temperatures can be found in the Supplementary Figs. S1–S10.

In Fig. 7 we can see that for interstitial type clusters, the smaller ones (<20) are reduced in number with an increase in temperature, while the

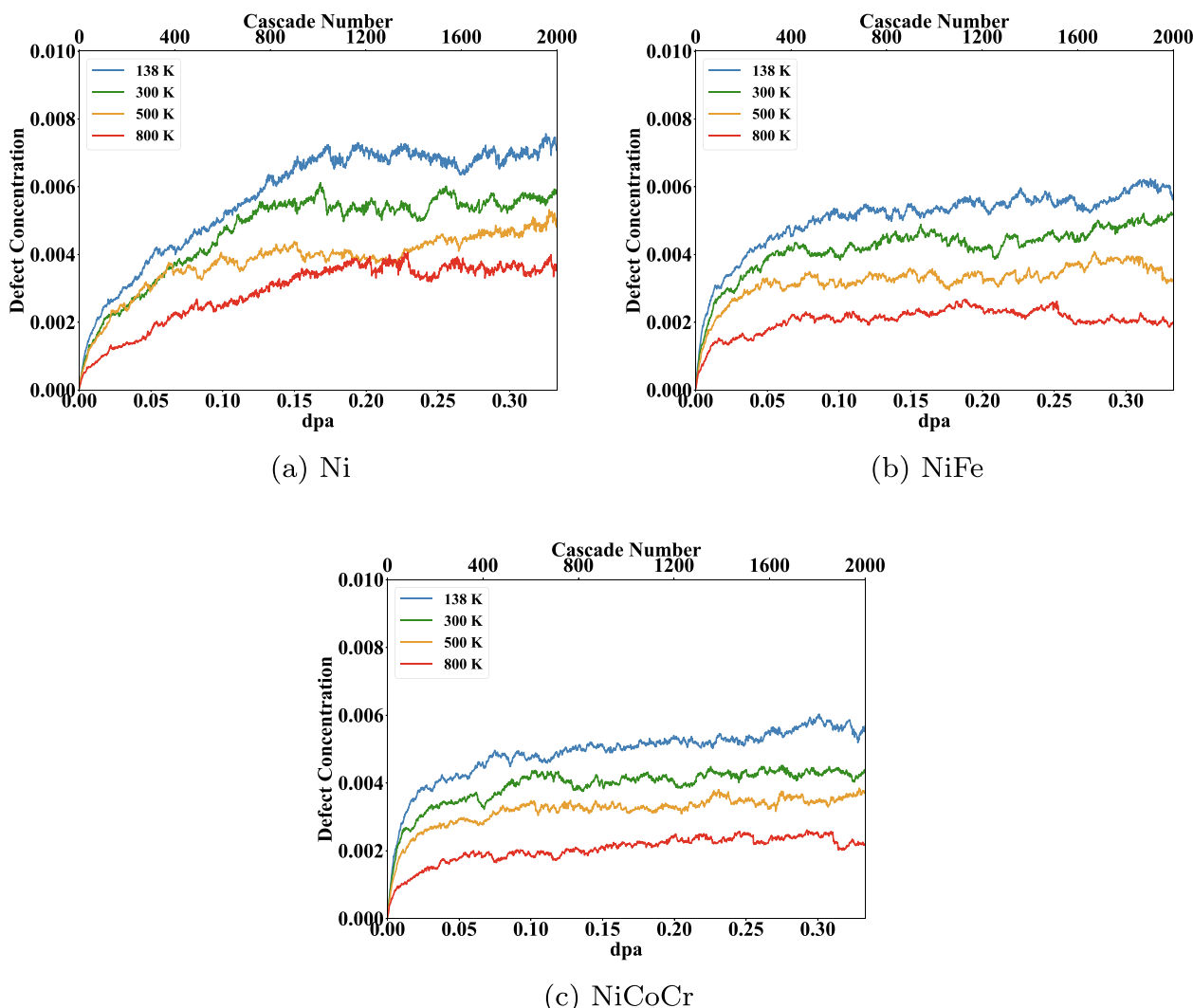


Fig. 2. Evolution of point defect concentration at different temperatures in Ni (a), NiFe (b) and NiCoCr (c) with the Zhou et al. potential.

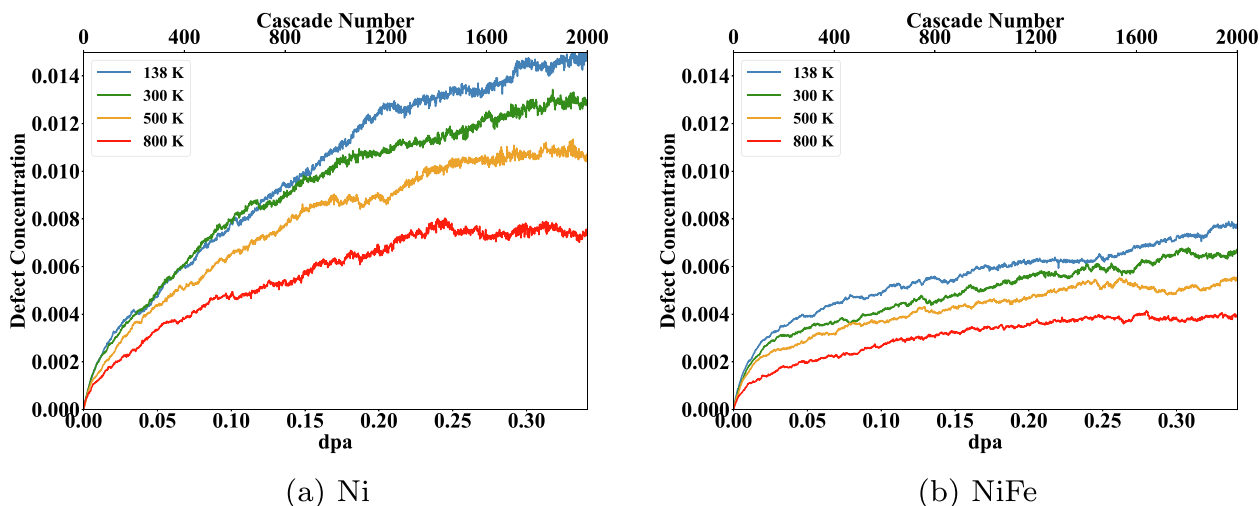


Fig. 3. Evolution of point defect concentration at different temperatures in Ni (a) and NiFe (b) using the Bonny et al. potential.

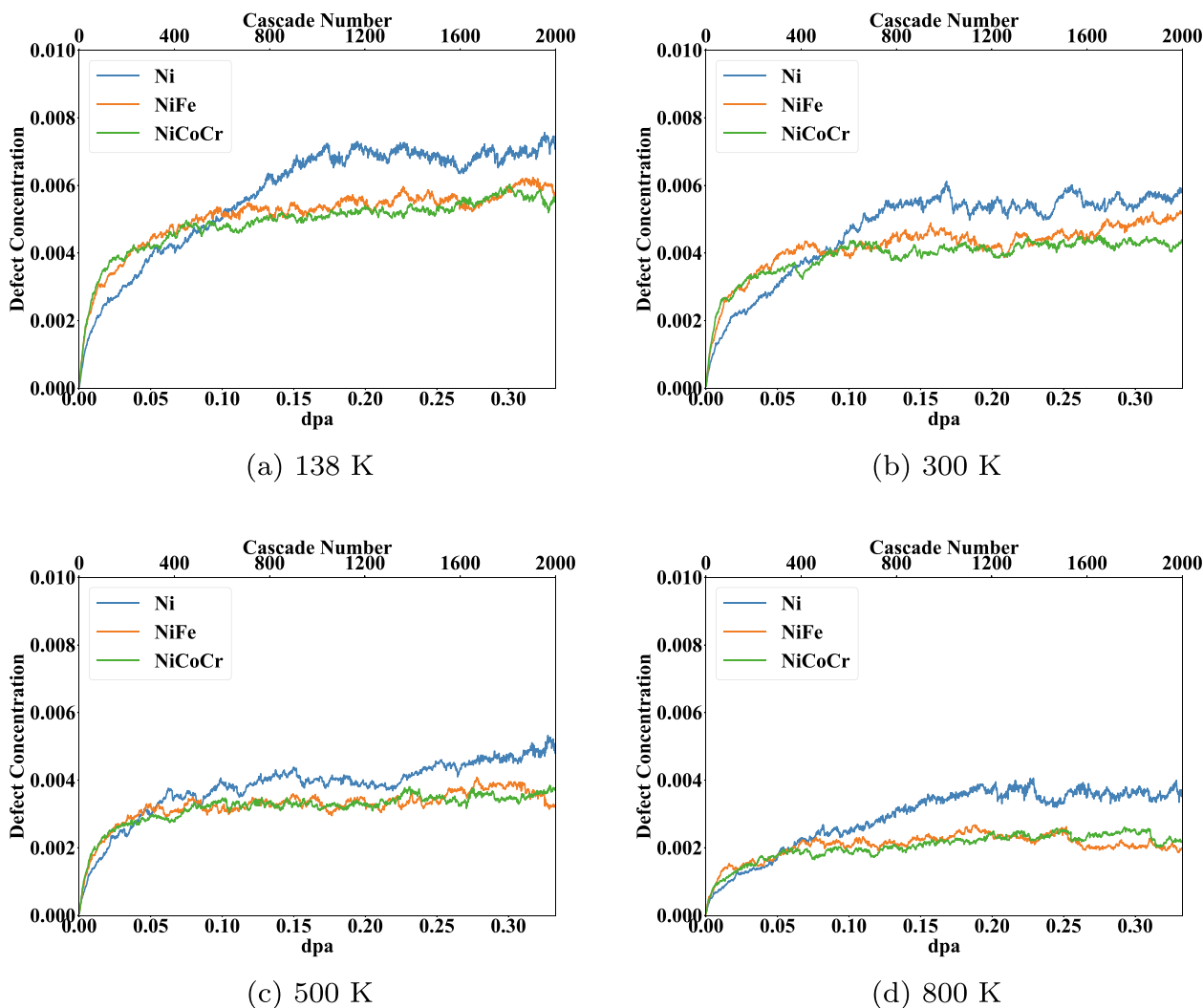


Fig. 4. Point defect concentration evolution comparison between materials at different temperatures with the Zhou et al. potential.

larger ones ( $>20$ ) are increased. When looking at the vacancy type clusters instead, there is an overall decrease at all sizes with the increase in temperature. Similar results can be seen for NiFe with the Zhou et al. potential in the [supplementary material, Figs. S3 and S4](#). Pure Ni on the

other hand ([Figs. S1 and S2](#)), have a decrease in all interstitial cluster sizes, while the larger ( $>10$ ) vacancy type clusters do not decrease as much as in NiFe and NiCoCr ([Figs. S3–S6](#)) with the increasing temperature.

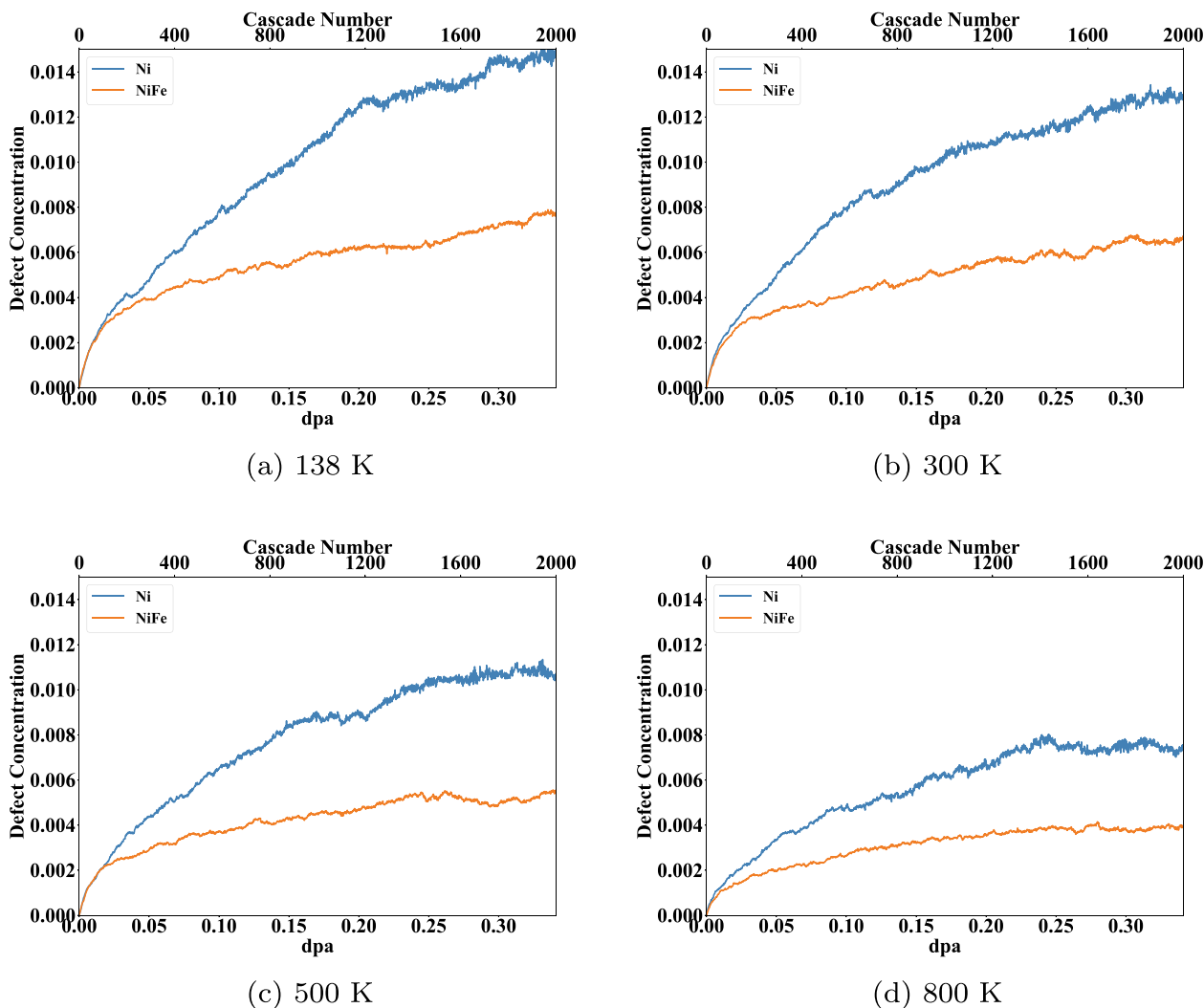


Fig. 5. Point defect concentration evolution comparison between materials at different temperatures with the Bonny et al. potential.

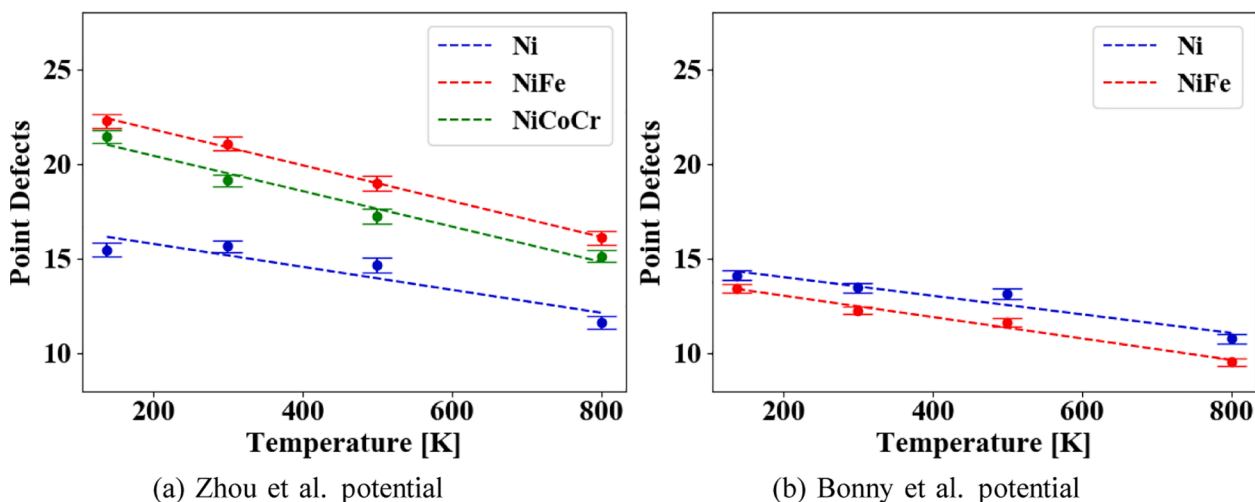


Fig. 6. Number of point defects produced in Ni, NiFe and NiCoCr by a single 5 keV collision cascade, in the 138 to 800 K temperature range, for both the Zhou et al. and Bonny et al. potentials.

When looking at the results in the materials using the Bonny et al. potential the results vary interestingly from the Zhou et al. counterparts. Comparing Bonny et al. Ni (Figs. S7 and S8) with Zhou et al. Ni (Figs. S1

and S2), we can see that for the Bonny et al. potential there is a lesser presence of the larger interstitial clusters (>20) over the whole temperature range. The same can be said for the vacancy type clusters.

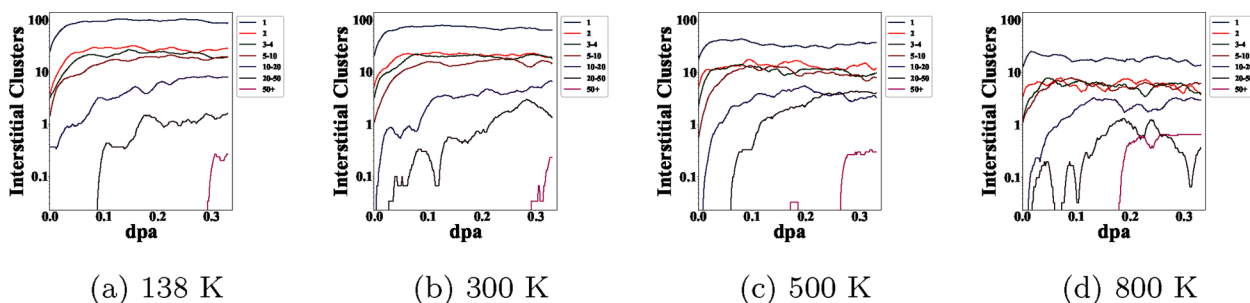


Fig. 7. Amount of differently sized interstitial clusters in NiCoCr for the Zhou et al. potential at different temperatures plotted against the irradiation dose. The sizes (in number of point defects) of the defect clusters are indicated in the legend.

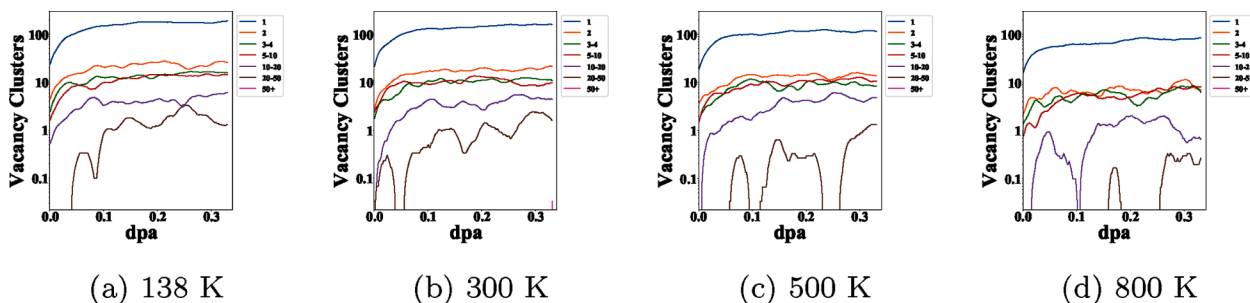


Fig. 8. Amount of differently sized vacancy clusters in NiCoCr for the Zhou et al. potential at different temperatures plotted against the irradiation dose. The sizes (in number of point defects) of the defect clusters is indicated in the legend.

When comparing Bonny et al. NiFe (Figs. S9 and S10), we can observe the same trend, with the addition that there are not any very large defect clusters ( $>50$ ) in the case of the Bonny et al. NiFe, while in the Zhou et al. NiFe there exists large clusters of both interstitial and vacancy type. Comparing Ni with the alloys in both materials, one can clearly see that there is a more pronounced presence of larger interstitial clusters ( $>20$ ) in the pure Ni for all temperatures.

### 3.3. Elemental point defect segregation

Supplementary Figs. S11-S13 show the concentration of elements in differently sized interstitial clusters, over the increasing dose. From Fig. S11 we see that the smaller defect clusters for the Zhou et al. NiFe are more rich in Ni rather than Fe, and that this does not change notably with an increase in temperature. For larger defect clusters the concentration of elements closes in on 50/50. From Fig. S12 we see that for the small clusters Ni is the most abundant, Co being the next, and Cr the least abundant element, while the concentration is about 33/33/33 for the larger clusters. This trend does also not change too much over the whole temperature range. The Bonny et al. NiFe data seen in Fig. S13 differ clearly from the Zhou et al. NiFe. The trend is similar, with Ni being more abundant than Fe in smaller clusters, but the concentrations of the different elements are much closer to one another for all cluster sizes.

Looking at the relative differences in energies of the interstitial dumbbells in the different alloys, we can observe the same trend as in the segregation investigation. The results are given in Supplementary Tables. S1-S3. For the Zhou et al. potential and in NiFe, the Ni-Ni dumbbell is the most stable one, followed by the Ni-Fe dumbbell, and the least stable is the Fe-Fe dumbbell. The relative differences are of the order of a few tenths of an eV, enough to almost only observe Ni-Ni dumbbells in the NiFe alloy. In NiFe with the Bonny potential, we observe that the mixed dumbbell is the most stable one, followed by the Ni-Ni dumbbell. In this potential we observe a bit more Ni in the small defect clusters, which cannot immediately be explained by the energy differences. However, looking at the statistics of the dumbbells, we can see that

about 30% of the Ni-Fe dumbbells reorient to Ni-Ni dumbbells. In addition, a previous study showed that there is a very wide range of dumbbell energies [34], where the Ni-Ni dumbbell is more stable in certain environments. This is also seen in our simulations, as the error bars (statistical variation) are much higher for the Bonny et al. potential compared to the error bars for the Zhou et al. potential. In NiCoCr we can observe that the Ni-Ni, Ni-Co and Co-Co dumbbells are more stable than the ones containing Cr. Of these more stable ones, the ones containing Ni are even more stable, which explains why most of the small interstitial clusters are mainly Ni rich but also a large fraction of Co is seen.

### 3.4. Dislocation evolution

Dislocation network snapshots from the irradiation simulations after 2000 cascades of one case for all materials at all temperatures can be seen in Figs. 9 (Zhou et al.) and 10 (Bonny et al.). The evolution of the dislocation networks for one case of all materials at all temperatures can be viewed in the supplementary material (Figs. S14-S18), as snapshots taken at 500 cascade increments, starting at the 500th cascade.

The 300 K case using the Zhou et al. potential shows similar results as in previous work [4]: Large Shockley partial dislocation chains, Frank loops and stacking fault tetrahedra (SFTs) in pure Ni, and several smaller Shockley partial dislocation clusters that might be connected and some stair-rod dislocation segments in NiFe and NiCoCr. The same dislocation types are consistent at all temperatures, but the amount of dislocation segments clearly reduces towards the higher temperatures.

The dislocation types differ somewhat for the Bonny et al. potential, when comparing to for the Zhou et al. potential. Both Ni and NiFe have a notable amount of small Frank loops, while there were only some large ones (if any) in Ni and none in NiFe for the Zhou et al. potential. The dislocation structures in Ni also seem smaller in size with the Bonny et al. potential, at the lower irradiation doses. These differences might be connected to a differing dislocation mobility, due to the different potentials.

The mobilities for the 5 and 10 Å dislocation loops can be seen in

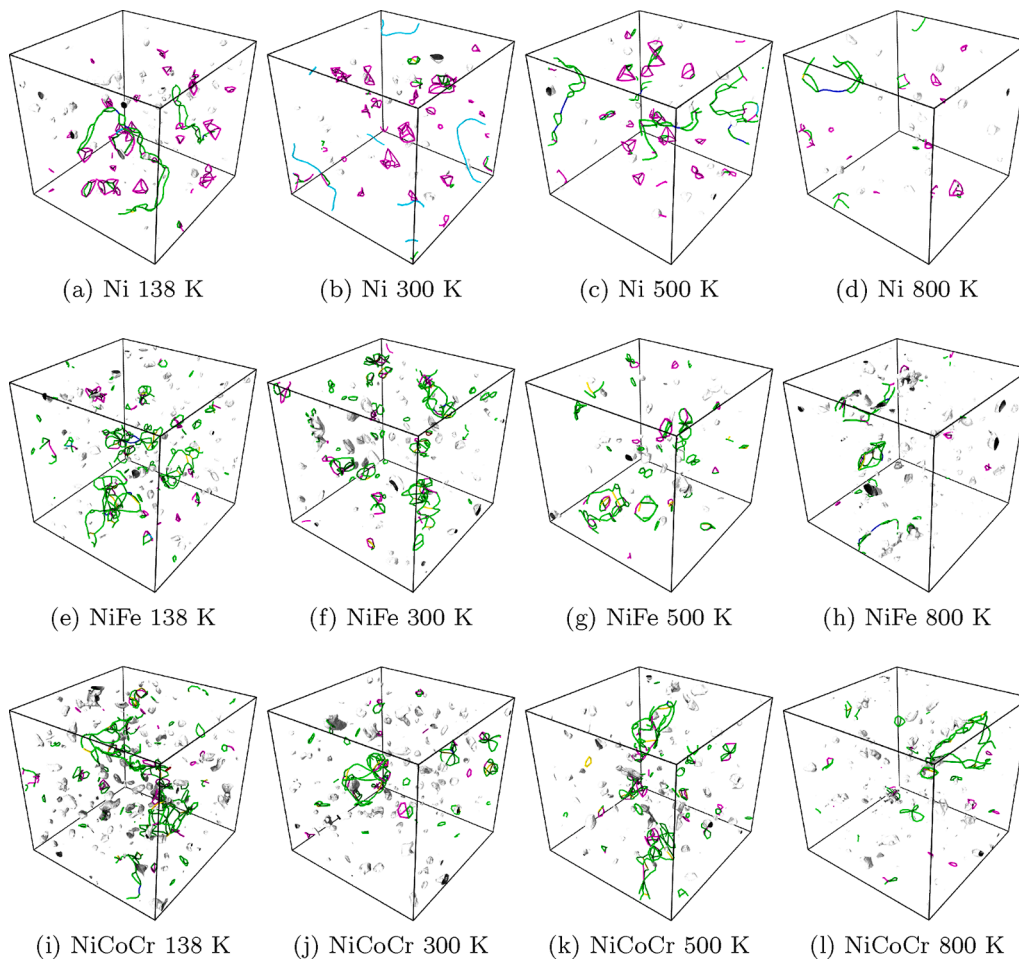


**Fig. 9.** Dislocation networks after 2000 cascades at different temperatures in Ni (a)–(d), NiFe (e)–(h) and NiCoCr (i)–(l) for the Zhou et al. potential.

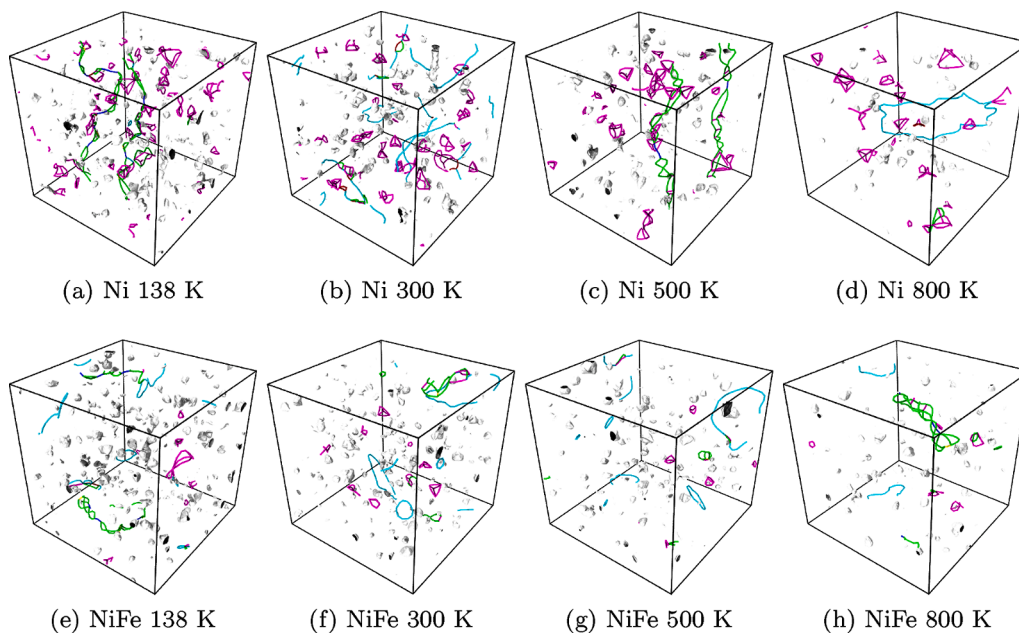


**Fig. 10.** Dislocation networks after 2000 cascades at different temperatures in Ni (a)–(d) and NiFe (e)–(h) with the Bonny et al. potential.

Fig. 11 for the Zhou et al. potential and Fig. 12 for the Bonny et al. potential. For the Zhou et al. potential we can see that the dislocation loops are mobile for both temperatures in Ni, while they are not in NiFe

and NiCoCr. The Bonny et al. potential gives different results for the larger dislocation loop, which appears to be static in Ni, like all dislocation loops in NiFe. Only the smaller dislocation loop is mobile in Ni

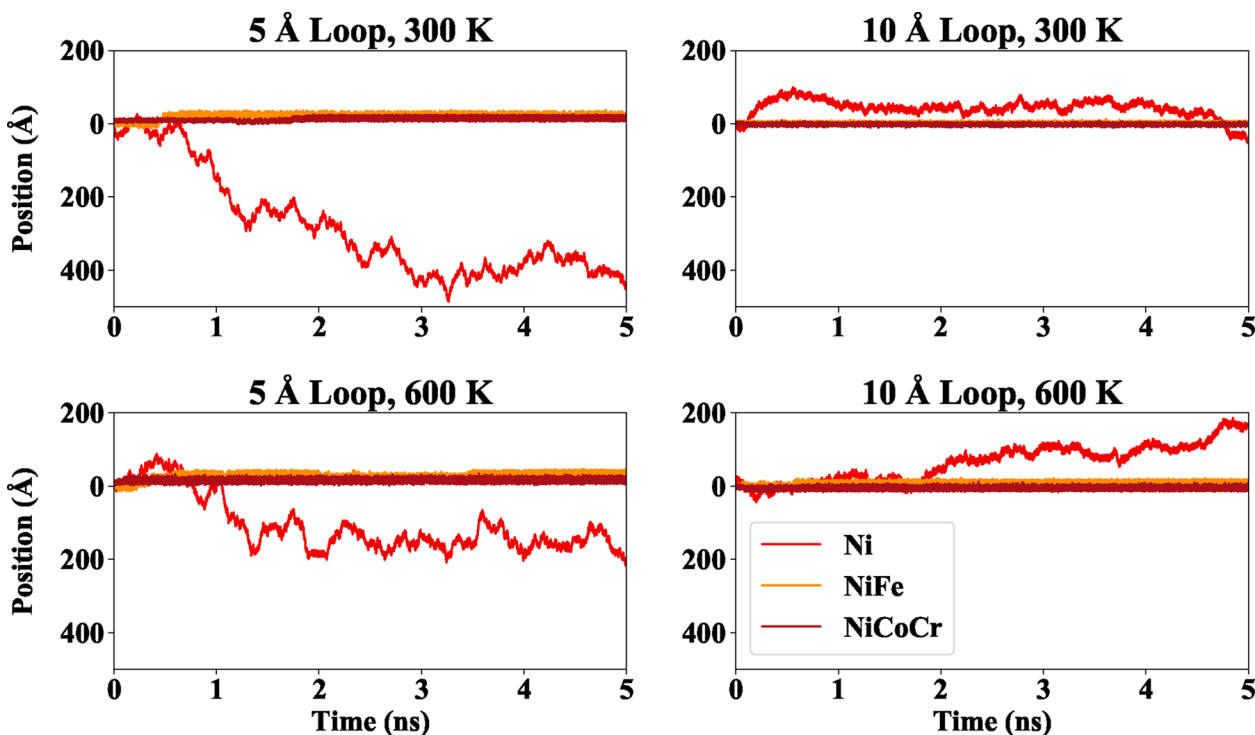


Fig. 11. Dislocation loop mobility using the Zhou et al. potential.

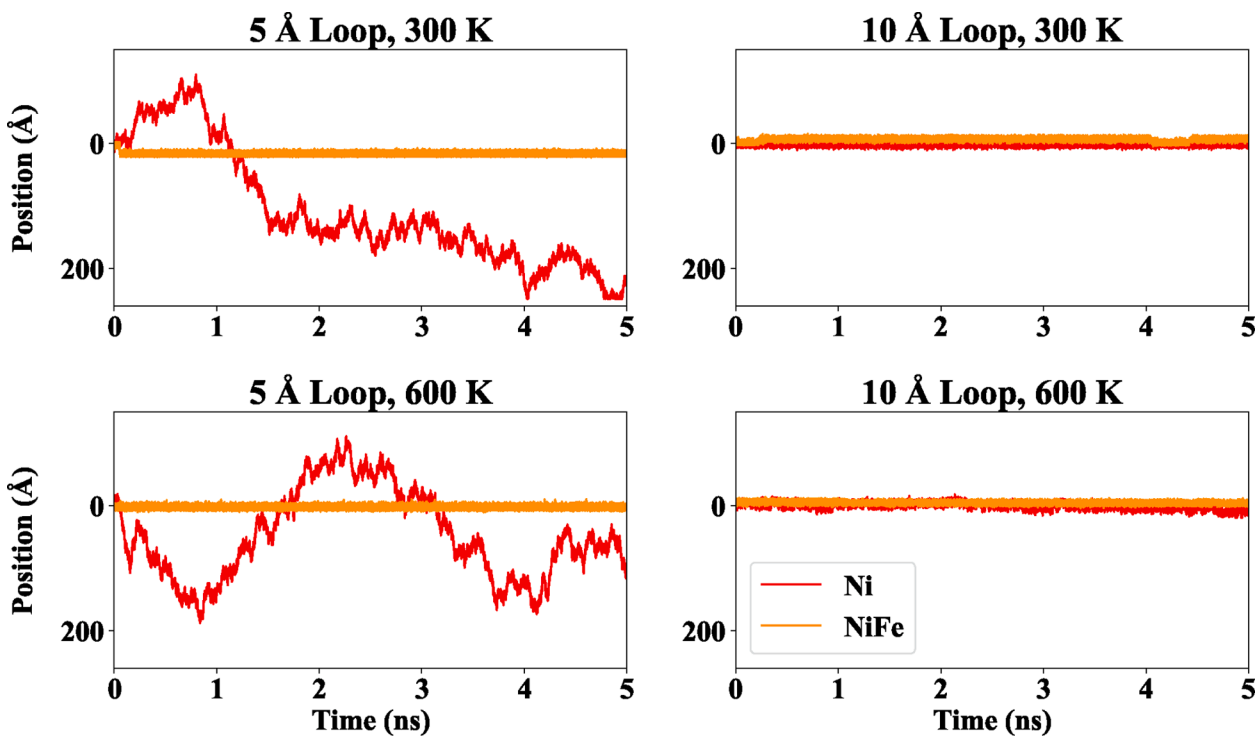


Fig. 12. Dislocation loop mobility using the Bonny et al. potential.

when using the Bonny et al. potential.

### 3.5. RBS/c calculations

Figs. 13 and 14 show the simulated RBS/c damage profiles for all materials at all temperatures. Pure and randomized Ni samples were also analyzed for each temperature in order to get a frame of reference for the

damage profiles (the “pristine” and “random” plots), and to obtain results which can directly be compared with experiments. The individual plots should be interpreted so that a higher count corresponds with a higher susceptibility to irradiation damage in a material, as the RBS/c detects disorder (atoms off the perfect structure lattice planes) in a crystalline material.

The damage profiles for the cells that have been simulated with the

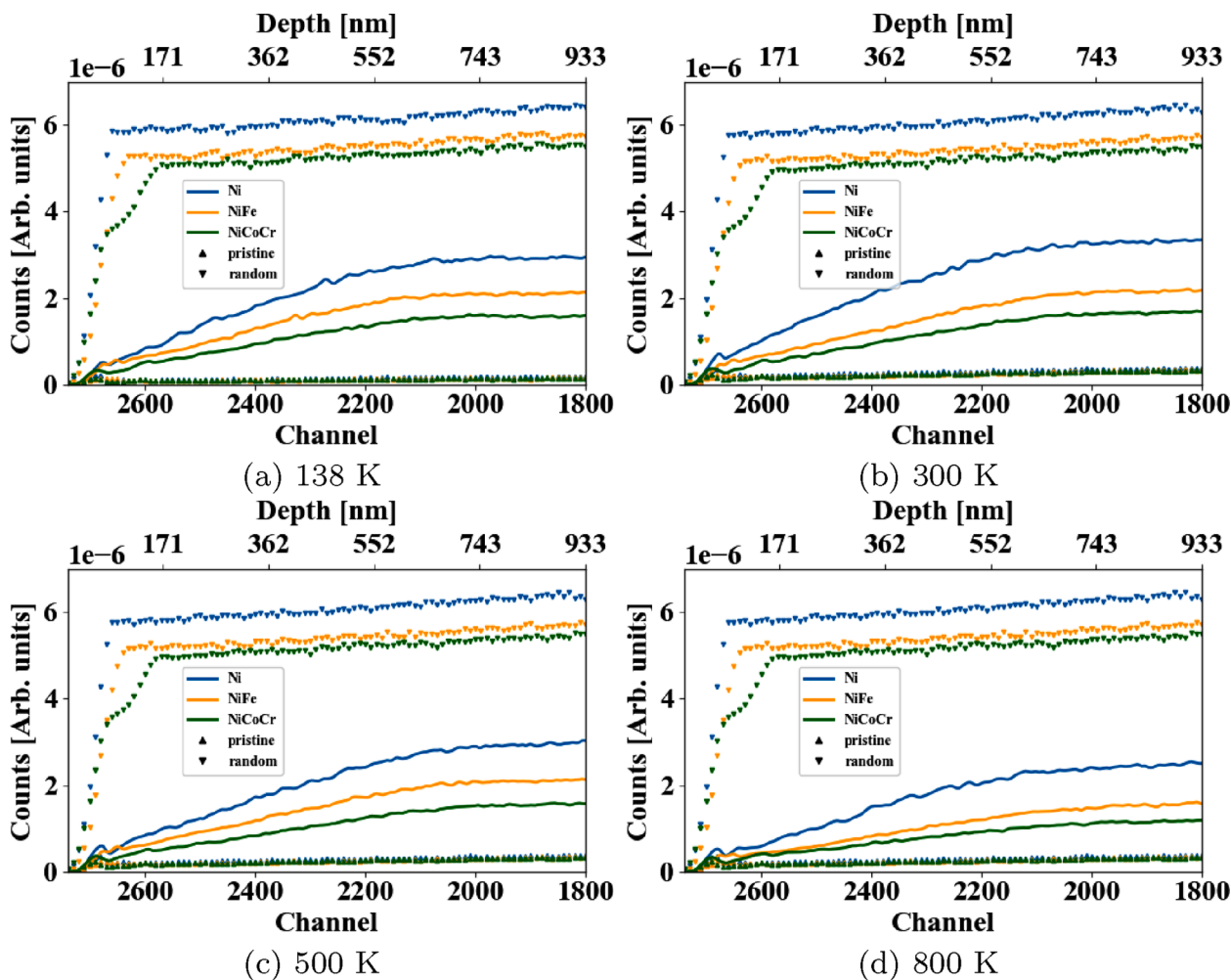


Fig. 13. RBS/c damage profiles for materials using the Zhou et al. potential.

Zhou et al. potential show the same ordering in damage build-up as seen before, i.e. Ni, NiFe, NiCoCr (from highest to lowest), at 138, 300, 500 and 800 K.

The damage profiles for the cells simulated with the Bonny et al. potential show consistent results, where NiFe outperforms Ni at every temperature by showing less counts throughout the slab. What is similar between the potentials is the fact that the alloys have less counts than pure Ni, and that the counts decrease a little with increase in temperature.

Relative disorders were also plotted based on the RBS/c spectra with the help of an iterative method presented in Ref. 35. The relative disorders can be found in the supplementary material (Figs. S21 and S22). These results are not presented in more detail here, but are mentioned due to them being a common method of representing the damage profiles of irradiated materials.

## 4. Discussion

### 4.1. Results of different defect analyses

The lowered defect accumulation corresponding with the increase in temperature seen in Figs. 2 and 3 is naturally expected due to a higher recombination rate of interstitial and vacancy type defects at higher temperatures. However, normally this recombination is assumed to occur due to long-time scale thermal defect migration. In the current case, it is interesting to note that even though the time between cascades is so short that there is practically no time to reach equilibrium through

thermally activated migration, we still observe a strong temperature dependence. From the same figures, we can also see that the saturation level of defect concentration is higher in pure Ni than the EAMC-alloys at all temperatures. This is a promising result, showing that the alloys withstand higher doses of irradiation damage, in terms of point defect accumulation, than pure Ni. This can be seen with more clarity in Figs. 4 and 5. In the same figures, it can also be seen that for the Zhou et al. potential, the point defect evolution is very similar for NiFe and NiCoCr in the high temperature range ( $\geq 500$  K). This makes it impossible to say which material performs better, in terms of lesser defect accumulation. This is an interesting result, especially when taking into account Ref. 11, where it is stated that NiFe appears to have a superior irradiation resistance when compared to NiCoCr at 500 K. However, results in Ref. 13 show a trend where NiFe is above NiCoCr in terms of perfect and Frank loop density at 773 K. This makes the choosing of alloying elements in EAMC-alloys and HEAs a more complicated task in high and wide temperature range applications, since the difference in performance between NiFe and NiCoCr seems overlapping.

The defect cluster analysis gives us insight in the interstitial and vacancy cluster size evolution, as well as the elemental constituents of interstitial clusters, over a wide temperature range, and shows interesting differences between materials simulated with the Zhou et al. and Bonny et al. potentials. The differences in the size evolution and segregation of elements in clusters stem mainly from the different ways the potentials model defect formation and mobility, as well as their handling of the overlapping cascades. For example, 10 Å interstitial loops showed to be much more mobile for the Zhou et al. Ni than for the Bonny et al. Ni

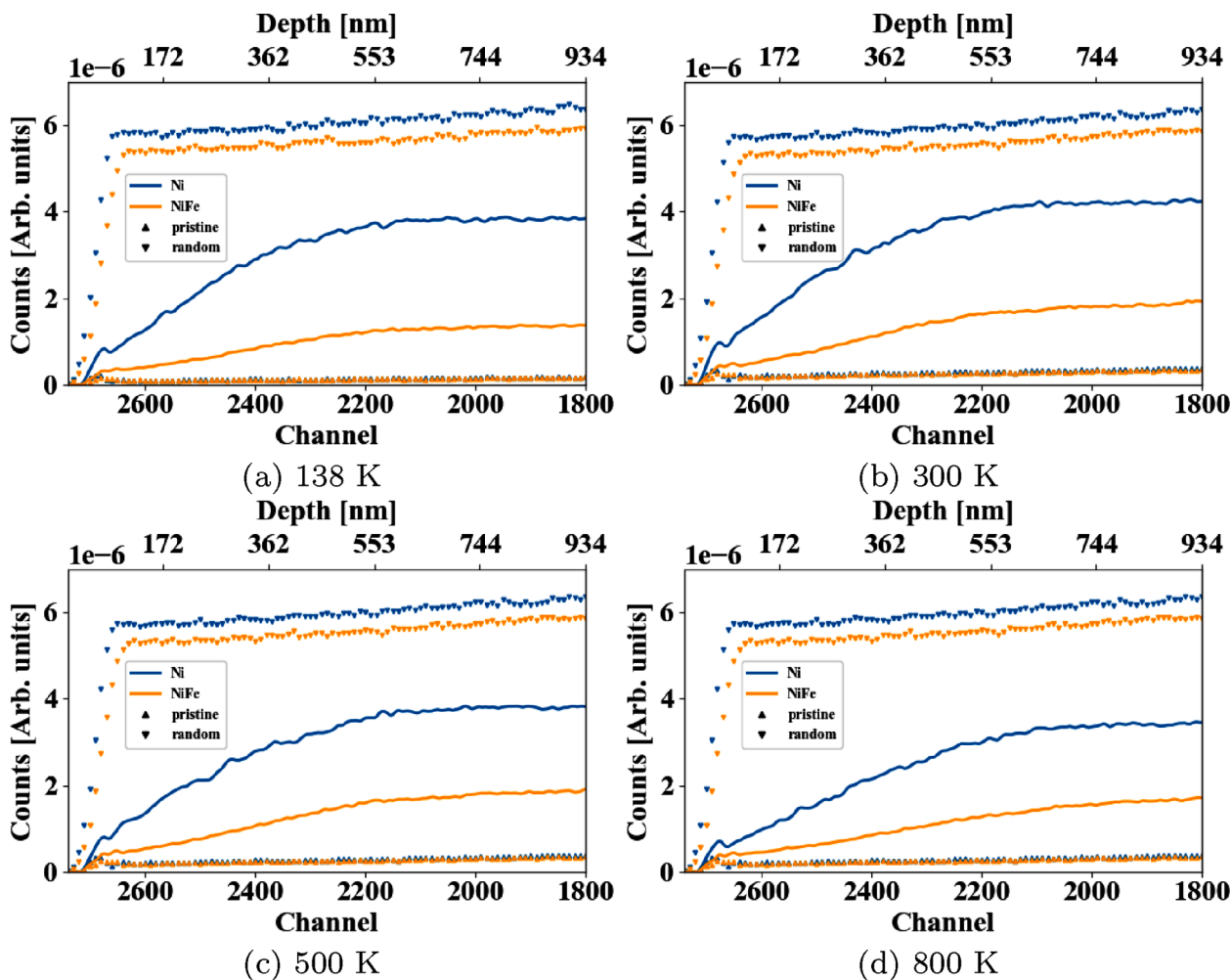


Fig. 14. RBS/c damage profiles for materials using the Bonny et al. potential.

in our dislocation loop mobility simulations (Figs. 11 and 12), which might indicate that larger defect cluster formation is more probable in Zhou et al. Ni than in Bonny et al. Ni. Then by comparing supplementary Figs. S1 and S7, we can indeed see that the larger interstitial clusters (>20, but especially the 50+) are, at temperatures less than 800 K, conceived earlier in the Zhou et al. Ni, than in the Bonny et al. Ni. Looking at the size evolution of the clusters from a perspective of increasing amount of alloying elements, we could also see that there was a decrease in larger interstitial clusters (compare Ni, NiFe, and NiCoCr, Figs. S1, S3 and 7). This can also be explained by a lesser defect mobility in the alloys by looking at the dislocation loop mobility in this work, Fig. 11, or previous work Ref. 3. The defect mobilities are also the main reason to the differences in the dislocation structures seen in the supplementary Figs. S17 and S18.

The study of elemental segregation in clusters showed that Ni is more abundant in smaller interstitial clusters in NiFe for both potentials (albeit, there was a difference in the magnitude of that abundance), while Ni is most abundant, Co second, and Cr the least abundant in NiCoCr. The larger interstitial clusters had a more even distribution of the different elements. These findings were supported by the interstitial dumbbell stability study, and affects the rest of the findings in this work regarding defect formation, evolution and migration in the studied materials.

#### 4.2. Rutherford backscattering analysis

The novel RBS/c analysis, using the RBSADEC code, showed to be

very powerful in acquiring damage profiles for our irradiated simulation cells. We first note that while the point defect concentration analysis (Figs. 2 and 3) show defect concentrations always below 0.01, the RBS/c curves appear to be significantly above their corresponding perfect levels (Figs. 13 and 14). This apparent discrepancy is explained by the RBS/c signal being very sensitive to the strain field from extended defects [30].

The 300 K case (Fig. 13(b)) with the Zhou et al. potential showed the same trend in terms of most damaged to least damaged (Ni, NiFe and NiCoCr) as has been seen before in both simulations and experiment, Ref. 31. The same trend was also seen in the 138, 500 and 800 K Zhou et al. cases, Figs. S19 (a), (c) and (d), and for all temperatures with the Bonny et al. potential, Fig. 14 and supplementary Fig. S20. To explain this ordering one does not need to look any further than to the discussion above regarding the defect analysis. Pure Ni shows in most cases a much higher point defect concentration than NiFe, which in turn has in most cases a higher point defect concentration than NiCoCr. In addition to this, the RBS/c method is especially sensitive to extended defects rather than point defects as explained in Ref. 30. Looking at the defect cluster sizes, we saw that Ni has the largest amount of large interstitial clusters, then comes NiFe, and last comes NiCoCr. This goes hand in hand with the trends that we observe in our RBS/c calculations.

The RBS/c results produced using the Bonny et al. potential, seen in Fig. 14 (and in the supplementary material Fig. S20), show clearly Ni as more damaged than NiFe for all temperatures. When comparing the Zhou and Bonny et al. damage profiles, one can see that there is a much larger gap between the Ni and NiFe curves. This difference is expected

when one takes into account the very different point defect concentrations, defect cluster sizes, dislocation structures, and dislocation mobilities in the different potentials.

All in all, the RBS/c results are very useful due to their comparability with experiments. Before, in similar irradiation simulations, Refs 2 and 4, the point defect concentration has been the point of focus in terms of radiation damage, but is very difficult to compare directly with experiments. The introduction of the RBSADEC code as an analysis tool makes a direct comparison between our irradiation simulation cells and irradiated experimental samples possible. All one needs to do is assure that the simulated dose is large enough, and that the fluence used in choosing the cells for the slab is similar to that in the experiment. Then the data can be scaled so that the perfect and random curves in the RBS/c simulated damage profiles match the experimental ones. An example of this can be seen in Fig. 15. In this figure we can see the simulated RBS/c spectra for all materials at 300 K, compared to corresponding experimental data acquired from Ref. 2. The experimental data was the result of  $\text{Ni}^+$  ions with a deposition energy of 1.5 MeV and a fluence of  $2.0 \times 10^{14} \text{ cm}^{-2}$ , while our simulations used a fluence half of that. This should not be a problem, since most of the defect concentrations and structures have already more or less saturated after 0.1 dpa in our simulations. The simulated and experimental data have been plotted on top of each other, so that the random spectra coincide. The simulated data follow the left vertical axis, while the experimental data follows the right vertical axis. From the graph we can see that the simulated materials follow the same trend with experiment in terms of most counts to the least. When inspecting the materials a bit closer we can see the following: Ni is overestimated by both the Zhou et al. and Bonny et al. potentials, albeit Zhou is a lot closer than Bonny. This is probably because the Bonny et al. Ni is the only case where the defect amount actually has not saturated for the dose range we are dealing with. The simulated spectra for NiFe follow the experimental one quite well, with the Bonny et al. spectrum having an almost one to one similarity. NiCoCr is also overestimated by the simulated spectra, similarly as in Ref. 2. Even though the spectra for NiFe is better described with the Bonny et al. potential, it might be better to use the Zhou et al. potential for massively overlapping cascade simulations due to overall better agreement between spectra.

The overall good agreement with experiments is remarkable in that molecular dynamics cannot (due to the limited timescale that is simulated inherent to the method) account for thermally activated point defect mobility between irradiation events. The observation that the simulated and experimental damage levels agree in all cases within 50% or better indicates that thermally activated defect migration does not play a major role for damage buildup after extended defect buildup has started. Most likely this is because at higher damage levels, any new point defects that are created in cascades, are absorbed in a nearby extended defect after only a few migration steps.

## 5. Conclusions

The main takeaways from this comprehensive look into irradiation damage in pure Ni, and NiFe and NiCoCr EAMC-alloys can be summarized as follows:

- The irradiation tolerance can be seen to be superior in the EAMC-alloys in a broad temperature range (138–800 K) compared to pure Ni, based on the previously much used point defect analysis and the novel RBS/c analysis using the RBSADEC code.
- The RBS/c analysis results agree well with experiments even though the simulations do not account for long time scale point defect migration.
- Differences in irradiation damage between the Zhou et al. and Bonny et al. potentials were studied in terms of point defects, defect clusters and dislocation structures, and were partly explained by interstitial dumbbell stability and dislocation loop mobility calculations.

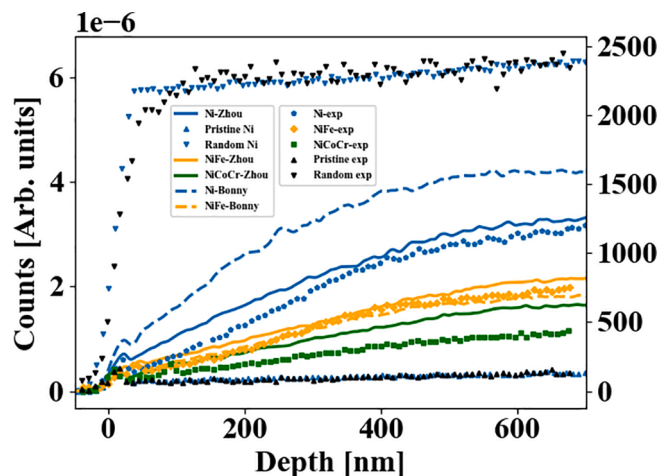


Fig. 15. Comparison between simulated and experimental RBS/c spectra at 300 K.

In addition to the three points above, the novel RBS/c analysis makes it possible to directly compare our irradiation simulations with experimentally irradiated samples. This can be particularly useful in aiding experimental techniques to acquire knowledge of the atomistic structure of defect clusters in various materials.

## Data availability

The raw/processed data required to reproduce these findings cannot be shared at this time due to technical or time limitations.

## CRediT authorship contribution statement

**Emil Levo:** Investigation, Formal analysis, Data curation, Writing - original draft, Writing - review & editing, Visualization. **Fredric Granberg:** Conceptualization, Formal analysis, Supervision, Writing - review & editing. **Kai Nordlund:** Conceptualization, Software, Writing - review & editing, Supervision, Project administration, Funding acquisition. **Flyura Djurabekova:** Conceptualization, Writing - review & editing, Supervision, Project administration.

## Declaration of Competing Interest

The authors declare that they have no known competing financial interests or personal relationships that could have appeared to influence the work reported in this paper.

## Acknowledgement

This work has partially been carried out within the framework of the EUROfusion Consortium and has received funding from the Euratom research and training programme 2014–2018 and 2019–2020 under grant agreement No 633053. The views and opinions expressed herein do not necessarily reflect those of the European Commission. Computer time granted by the IT Center for Science – CSC – Finland and the Finnish Grid and Cloud Infrastructure persistent identifier urn:nbn:fi:research-infras-2016072533 are gratefully acknowledged.

## Appendix A. Supplementary data

Supplementary data associated with this article can be found, in the online version, at <https://doi.org/10.1016/j.commatsci.2021.110571>.

## References

- [1] J. Yeh, S. Chen, S. Lin, J. Gan, T. Chin, T. Shun, C. Tsau, S. Chang, Nanostructured high-entropy alloys with multiple principal elements: novel alloy design concepts and outcomes, *Advanced Engineering Materials* 6 (5) (2004) 299–303.
- [2] F. Granberg, K. Nordlund, M.W. Ullah, K. Jin, C. Lu, H. Bei, L.M. Wang, F. Djurabekova, W.J. Weber, Y. Zhang, Mechanism of radiation damage reduction in equiatomic multicomponent single phase alloys, *Physical Review Letters* 116 (13) (2016), 135504.
- [3] F. Granberg, F. Djurabekova, E. Levo, K. Nordlund, Damage buildup and edge dislocation mobility in equiatomic multicomponent alloys, *Nuclear Instruments and Methods in Physics Research Section B* 393 (2017) 114–117.
- [4] E. Levo, F. Granberg, C. Fridlund, K. Nordlund, F. Djurabekova, Radiation damage buildup and dislocation evolution in Ni and equiatomic multicomponent Ni-based alloys, *Journal of Nuclear Materials* 490 (2017) 323–332.
- [5] E. Levo, F. Granberg, D. Utt, K. Albe, K. Nordlund, F. Djurabekova, Radiation stability of nanocrystalline single-phase multicomponent alloys, *Journal of Materials Research* 34 (5) (2019) 854–866.
- [6] S. Xia, X. Yang, T. Yang, S. Liu, Y. Zhang, Irradiation resistance in  $Al_xCoCrFeNi$  high entropy alloys, *The Journal of The Minerals, Metals & Materials Society* 67 (10) (2015) 2340–2344.
- [7] N.K. Kumar, C. Li, K. Leonard, H. Bei, S. Zinkle, Microstructural stability and mechanical behavior of FeNiMnCr high entropy alloy under ion irradiation, *Acta Materialia* 113 (2016) 230–244.
- [8] C. Lu, L. Niu, N. Chen, K. Jin, T. Yang, P. Xiu, Y. Zhang, F. Gao, H. Bei, S. Shi, et al., Enhancing radiation tolerance by controlling defect mobility and migration pathways in multicomponent single-phase alloys, *Nature Communications* 7 (2016) 13564.
- [9] G. Velisa, M.W. Ullah, H. Xue, K. Jin, M.L. Crespillo, H. Bei, W.J. Weber, Y. Zhang, Irradiation-induced damage evolution in concentrated Ni-based alloys, *Acta Materialia* 135 (2017) 54–60.
- [10] M.W. Ullah, H. Xue, G. Velisa, K. Jin, H. Bei, W.J. Weber, Y. Zhang, Effects of chemical alternation on damage accumulation in concentrated solid-solution alloys, *Scientific Reports* 7 (1) (2017) 4146.
- [11] G. Velisa, Z. Fan, M. Crespillo, H. Bei, W. Weber, Y. Zhang, Temperature effects on damage evolution in ion-irradiated nickel concentrated solid-solution alloy, *Journal of Alloys and Compounds* (2020) 154918.
- [12] Z. Fan, G. Velisa, K. Jin, M.L. Crespillo, H. Bei, W.J. Weber, Y. Zhang, Temperature-dependent defect accumulation and evolution in Ni-irradiated NiFe concentrated solid-solution alloy, *Journal of Nuclear Materials* 519 (2019) 1–9.
- [13] S. Shi, M.-R. He, K. Jin, H. Bei, I.M. Robertson, Evolution of ion damage at 773K in Ni-containing concentrated solid-solution alloys, *Journal of Nuclear Materials* 501 (2018) 132–142.
- [14] K. Nordlund, M. Ghaly, R.S. Averback, M. Caturla, T. Diaz de la Rubia, J. Tarus, Defect production in collision cascades in elemental semiconductors and fcc metals, *Physical Review B* 57 (13) (1998) 7556–7570.
- [15] K. Nordlund, J. Keinonen, M. Ghaly, R.S. Averback, Coherent displacement of atoms during ion irradiation, *Nature* 398 (6722) (1999) 49–51.
- [16] X. Zhou, R. Johnson, H. Wadley, Misfit-energy-increasing dislocations in vapor-deposited CoFe/NiFe multilayers, *Physical Review B* 69 (2004), 144113.
- [17] G. Bonny, N. Castin, D. Terentyev, Interatomic potential for studying ageing under irradiation in stainless steels: the FeNiCr model alloy, *Modelling and Simulation in Materials Science and Engineering* 21 (8) (2013), 085004.
- [18] Z. Lin, R.A. Johnson, L.V. Zhigilei, Computational study of the generation of crystal defects in a bcc metal target irradiated by short laser pulses, *Physical Review B* 77 (214108) (2008), 214108.
- [19] J. Ziegler, SRIM-2013 software package, available online at <http://www.srim.org>. (2013).
- [20] J. Ziegler, J. Biersack, U. Littmark, *The Stopping and Range of Ions in Matter*, Pergamon, New York, 1985.
- [21] H.J.C. Berendsen, J.P.M. Postma, W.F. van Gunsteren, A. DiNola, J.R. Haak, Molecular dynamics with coupling to external bath, *The Journal of Chemical Physics* 81 (8) (1984) 3684.
- [22] G. Kinchin, R. Pease, The displacement of atoms in solids by radiation, *Reports on Progress in Physics* 18 (1) (1955) 1.
- [23] M.T. Robinson, I.M. Torrens, Computer simulation of atomic-displacement cascades in solids in the binary-collision approximation, *Physical Review B* 9 (12) (1974) 5008.
- [24] M. Norgett, M. Robinson, I. Torrens, A proposed method of calculating displacement dose rates, *Nuclear Engineering and Design* 33 (1) (1975) 50–54.
- [25] K. Nordlund, S.J. Zinkle, A.E. Sand, F. Granberg, R.S. Averback, R. Stoller, T. Suzudo, L. Malerba, F. Banhart, W.J. Weber, F. Willaime, S.L. Dudarev, D. Simeone, Improving atomic displacement and replacement calculations with physically realistic damage models, *Nature Communications* 9 (1) (2018) 1–8.
- [26] K. Nordlund, S.J. Zinkle, A.E. Sand, F. Granberg, R.S. Averback, R.E. Stoller, T. Suzudo, L. Malerba, F. Banhart, W.J. Weber, F. Willaime, S.L. Dudarev, D. Simeone, Primary radiation damage: A review of current understanding and models, *Journal of Nuclear Materials* 512 (2018) 450–479.
- [27] J. Nord, K. Nordlund, J. Keinonen, Amorphization mechanism and defect structures in ion beam amorphized Si, Ge and GaAs, *Physical Review B* 65 (2002), 165329.
- [28] A. Stukowski, Visualization and analysis of atomistic simulation data with OVITO—the Open Visualization Tool, *Modelling and Simulation in Materials Science and Engineering* 18 (1) (2010), 015012.
- [29] A. Stukowski, V. Bulatov, A. Arsenlis, Automated identification and indexing of dislocations in crystal interfaces, *Modelling and Simulation in Materials Science and Engineering* 20 (8) (2012), 085007.
- [30] S. Zhang, K. Nordlund, F. Djurabekova, Y. Zhang, G. Velisa, T. Wang, Simulation of rutherford backscattering spectrometry from arbitrary atom structures, *Physical Review E* 94 (4) (2016), 043319.
- [31] S. Zhang, K. Nordlund, F. Djurabekova, F. Granberg, Y. Zhang, T. Wang, Radiation damage buildup by athermal defect reactions in nickel and concentrated nickel alloys, *Materials Research Letters* 5 (6) (2017) 433–439.
- [32] K. Nordlund, Molecular dynamics simulation of ion ranges in the 1–100 keV energy range, *Computational materials science* 3 (4) (1995) 448–456.
- [33] K. Jin, W. Guo, C. Lu, M.W. Ullah, Y. Zhang, W.J. Weber, L. Wang, J.D. Poplawsky, H. Bei, Effects of Fe concentration on the ion-irradiation induced defect evolution and hardening in Ni-Fe solid solution alloys, *Acta Materialia* 121 (2016) 365–373.
- [34] S. Zhao, G.M. Stocks, Y. Zhang, Defect energetics of concentrated solid-solution alloys from ab initio calculations:  $Ni_{0.5}Co_{0.5}$ ,  $Ni_{0.5}Fe_{0.5}$ ,  $Ni_{0.8}Fe_{0.2}$  and  $Ni_{0.8}Cr_{0.2}$ , *Physical Chemistry Chemical Physics* 18 (34) (2016) 24043–24056.
- [35] Y. Zhang, J. Lian, Z. Zhu, W.D. Bennett, L.V. Saraf, J.L. Rausch, C.A. Hendricks, R. Ewing, W.J. Weber, Response of strontium titanate to ion and electron irradiation, *Journal of Nuclear Materials* 389 (2) (2009) 303–310.